Aircraft Measurements for Understanding Air-Sea Coupling and Improving Coupled Model Predictions

Qing Wang
Meteorology Department, Naval Postgraduate School
Monterey, CA 93943
Phone: (831) 656-7716, Fax: (831) 656-3061 email: qwang@nps.edu

Award # N0001413WX20025

Anthony Bucholtz
Naval Research Laboratory, 7 Grace Hopper Ave, Monterey, CA
phone: (831) 656-5024 fax: (831) 656-4769 email: anthony.bucholtz@nrlmry.navy.mil

Award # N0001413WX21204

LONG-TERM GOAL

The long-term goal of this project is to understand the coupled air-sea processes and improve physical parameterizations of the coupled model in various large-scale forcing conditions.

OBJECTIVES

The NOAA WP-3D efforts of DYNAMO/LASP intend to address critical issues in air-sea interaction processes in different stages of MJO events. The measurement objectives include 1) to make concurrent measurements of the atmosphere, surface, and the upper ocean for coupled air-sea interaction study; 2) to characterize convective processes and understand the complex feedback processes among surface forcing, cloud dynamics and thermodynamics, radiation, and environmental conditions in various phases of the MJO; 3) to extend point measurements on island and ships to a broader area near the DYNAMO region; and 4) To obtain a suite of measurements suitable for model evaluation/validation as well as data assimilations. In FY13, the objectives of our analyses of the WP-3D LASP measurements include: 1) extensive data QC of the AXBT/AXCTD data and analyses of the upper ocean characteristics in different phases of the MJO; 2) to characterize the atmospheric boundary layers observed in LASP in convective and non-convective conditions; 3) to understand the variation of air-sea coupling in different stages of the MJO.

The objectives of the NRL project are to obtain vertical profiles of the solar and IR irradiance throughout the atmospheric column in order to characterize the evolution of the solar and IR heating/cooling rate profiles for an MJO cycle. Also, to use the measured solar/IR irradiance profiles as input to, and validation of, the Navy's coupled ocean/atmosphere model, COAMPS. FY13 effort focused on data QC of the radiation measurements.

APPROACH

The WP-3D measurements produced large amount of data including the flight level data and data from expendables. Our FY13 effort mainly focused on analyses of the expendable data. In addition to extensive amount of work on data QC for the AXBT and AXCTD measurements, we also investigated the upper ocean characteristics from a large number of AXBT/AXCTD data. In addition, as one of the unique measurement strategy of LASP/DYNAMO WP-3D project was the concurrent and co-located atmosphere and upper ocean measurements through coordinated dropsonde and AXBT/AXCTD deployments, analyses of the data from dropsonde and AXBT/AXCTD pairs was a priority of our FY13 analyses. For all analyses, we separate the data into groups in different stages of the November 2011 MJO event. The measurements were also divided into categories of conditions under convective active activities (convection) and without convective influences (non-convection) based on satellite cloud imageries near the time of aircraft measurements.

Qing Wang is responsible for the overall WP-3D LASP project. Analyses of the LASP/DYNAMO data was also performed by NRC postdoc Denny Alappattu.

WORK COMPLETED

Specific work done in FY2013 are listed in the following.

1. Reprocessing of all AXBT and AXCTD measurements from LASP/DYNAMO, and extensive QC effort for AXCTD measurements to recover data without depth information and remove a depth bias using an objective approach based on spectrogram of the audio files. The quality controlled datasets were submitted to DYNAMO data archive.
2. Spatial and temporal variability of upper ocean properties were studied using AXBT/AXCTD measurements. This analyses include the top water thermal stratification, upper ocean heat content, depth of the ocean mixed layer.
3. Analyses of processes affecting the upper ocean temperature. This analyses make use of the satellite observed SST field, NCEP reanalyses field, as well as measurements of the Argo float in the DYNAMO southern domain.
4. Characterized the layering structure of the atmospheric boundary layer structure in clear and convective conditions from all dropsonde measurements.
5. Examined the air-sea temperature difference in different stages of MJO using the co-located dropsonde-AXBT/AXCTD pairs. This analyses revealed the variability of sensible heat flux in different stages of MJO that is different from those from TOGA COARE measurements on the western Pacific.
6. Analysis and quality-control of the NRL solar and IR broadband radiometer irradiance data from the NOAA P-3 aircraft was completed. QC'ed datasets, with documentation, of the solar and IR irradiance measured on each flight of the NOAA P-3 aircraft during DYNAMO were submitted to the NPS DYNAMO data archive and linked to the main UCAR DYNAMO Data Archive website.

RESULTS

AXCTD data QC: AXCTD raw measurements and realtime on-flight processing suffer from two major problems. One is the missing depth information, which occurred to about 30% of the AXCTD measurements, the other is the a depth bias which is seen in many of the AXCTD profiles, which varied from profile to profile. The first problem was solved using an updated processing software from the manufacture and the reprocess all the original audio files from each probe. For the depth bias problem, a commonly accepted approach is to remove the portion of data at the top subjectively. By

examining a large amount of datasets with and without the bias error, we have found an approach to objectively removed the depth bias through the spectrogram of the AXCTD audio signal. Depth biases in the AXCTD profiles results in erroneous estimation of mixed layer parameters and can lead to wrong interpretation of results. Figure 1 shows an example of the depth bias identified. Figure 2a shows the vertical cross section of temperature from the AXBTs and uncorrected AXCTD profiles taken along the diagonal transect from Diego Garcia (DG) to R/V Revelle (RV). Distances from DG are shown in the lower X-axis and upper X-axis represents the corresponding latitudes. Positions of AXBT and AXCTD drops relative to DG are shown by black and white dotted lines respectively in the figure. This vertical cross-section of temperature shows a wave-like structure in the mixed layer depth (MLD) and thermocline layer. Figure 2b shows the same temperature cross-section but using the depth bias corrected AXCTD profiles. The corrected data removed the erroneous wavy structure depicted in the previous figure. The presence of a dome structure in the thermocline due to the presence of Seychelles-Chagos thermocline ridge (SCTR) in the DYNAMO domain in apparent in the corrected data.

SST variability in different stages of MJO: We conducted ocean observations using AXBTs/AXCTDs along the DG to RV transect on 13, 22 and 26 November 2011. These dates are representatives of the 2011 November MJO (hereafter MJO2) evolution in stage1 (pre-active), stage 2 (onset), and stage 3 (active), respectively. Since the observations were on the same transect, it allows a direct comparison of the upper ocean thermodynamic properties. In Figure 3, we show the mean temperature of the upper 3 m of the ocean (loosely termed as SST) along the DG to RV transect for the different stages of MJO2. SST was the warmest during the stage 1 (blue curve) and more or less the same during the stage 2 (green curve). It was substantially cooler in stage 3 (red curve). Reduction in SST in stage 3 can be caused by various factors including changes in surface turbulent heat flux and decreased in solar radiating reaching the sea surface. Johnson and Ciecielski (2013) documented enhanced surface wind during stage 3 of MJO2 which may lead to larger surface heat loss. Average SST estimated from each transect were 29.8°C, 29.7°C and 29.1°C in stage 1, stage 2 and stage 3 respectively. Average SST cooling in the transition from sunny/calm phase (stage 1) to cloudy/windy phase (stage 3) was about 0.7°C. AXBT/AXCTD estimated SST shows that the sea surface was cooled more than 1°C during the entire cycle of MJO2, which is in good agreement with the TMI SST measurements (Fig. 4) . The amplitude of this SST cooling was large in comparison to earlier observations of 0.15°C reported for the tropical Indian Ocean (TIO; Shinoda et al., 1998). Compare to other MJO events in similar regions, the observed amplitude of SST variability in MJO2 can be considered as an intense upper ocean cooling event.

In Fig. 4 we show the SST field averaged over the DYNAMO domain (8°S-0° and 72°E-81°E) for the entire MJO2 cycle (from 10 November to 15 December) from various sources.Two observations that can be made from this figure, especially from satellite and in situ data are: (1) SSTs were at their peak magnitudes well before the onset of MJO2. Highest SSTs observed during 13 November to 17 November period in the stage 1 of MJO2. This means that SST build up did not take place all through the stage 1 until the onset (stage 2) or active (stage 3) phase of MJO2. Instead, SSTs showed the tendency to decrease from 18 November (in stage 1) onwards and became cooler in the stages 2 and 3. (2) Cooler SSTs persisted in the stage 4, even after the end of convective stage (stage 3) of MJO2. AXBT/AXCTD observations also support the TMI data but the magnitude was smaller. Observations of SST from the RAMA buoys at 90°E, 1.5°S (Johnson and Ciesielski 2013), 80.5°E, 1.5°S (Shinoda et al., 2013a), and 0°, 80.5°E (Moum et al., 2013) also corroborate these findings. SST increased to magnitudes equivalent to that of stage 1 only after 10 December. This implies that SST did not shoot

up abruptly soon after active MJO stage and sea surface maintained its cooler state for a few days more. Ocean heat content was also the lowest soon after the active stage of MJO2 (figure not shown).

Upper ocean heat content: Estimation of heat content is an efficient way to calculate the energy lost or gained by upper oceanic layer through various processes. Heat content of the MLD did not show much difference among stage 1, stage 2 and stage 3. Rather the MLD heat content showed the variability similar to MLD itself. We estimated the heat content in the water slabs of 0-30 m, 30-50 m and 50 m-100 m separately (Figs. 4a-c). Heat content in different stages of MJO2 in the 0-30 m layer closely resembled the SST variability (Fig. 3) with lowest heat content in stage 3. Heat content of stage 2 shows considerable latitudinal gradient with increase of OHC towards RV. In the 30-50 m layer heat content did not show considerable difference among the three stages of MJO2. Heat content in the 50-100 m depth range largely varies with the depth of the thermocline. Heat content was the minimum in the core region of thermocline ridge (~400 km to ~900 km). It can be seen that the stage 1 heat content was marginally higher in the 600 km-900 km range. This shows that the thermocline was slightly warmer in stage 1 in comparison to stage 2 and stage 3. Since heat content usually shows more direct relationship to heat flux forcing than mixed layer depth, it is considered as a more consistent, more robust, and less noisy measure of upper ocean variability than other quantities such as temperature (Stephenson et al., 2012). It may be noted that the SST variability observed among the three stages of MJO2 is reflected directly in a thin layer of upper 30 m. Thus, heat content of the upper 30 m represents the effects due to both surface fluxes and subsurface processes.

Figure 6 shows the upper 30 m mean heat content on the observation days estimated from AXBT/AXCTD. Mean upper ocean heat content increased from ~3.50 GJ m^{-2} to ~3.58 GJ m^{-2} from 11 November to 22 November period in the stage 1. Thereafter, heat content showed a decreasing trend during stages 2 and 3. But it is interesting to see that heat content was the lowest in the stage 4 (4 and 8 December), after the active MJO2 convection. Heat content showed a recovering trend to higher values only on 13 December. Behavior of heat content in stage 4 requires further attention.

Roles of surface flux and subsurface processes: Figure 7 shows the domain averaged net long-wave radiation (NLWR), sensible heat flux (SHF) and latent heat flux (LHF) from 10 November to 15 December from NCAR-NCEP reanalysis. These are negative quantities and are responsible for heat loss from ocean. SHF was very small in comparison with LHF and show little variation during different stages of MJO2. Although NLWR was greater than SHF it also did not show considerable variation during MJO2 when compared to latent heat flux (blue curve). LHF dominates the factors responsible for heat loss from the ocean. Maximum wind and magnitude of maximum latent heat flux coincided on November 29 in the stage 3 of MJO2. This confirms the wind speed as the major component that determines the latent heat loss during MJO2. At the beginning of stage 2 latent heat loss was ~-85 W m^{-2}. This increased to ~-220 W m^{-2} on 29 November in stage 3. But soon after the active stage of MJO2 latent heat loss decreased and became ~-85 W m^{-2} on 4 December. This latent heat flux value was equivalent to that observed on the beginning of stage 2. Latent heat loss from ocean surface increased again to ~-160 W m^{-2} on 7 December. High SSTs observed during the stage1 and cooler SSTs during stage 2 can be understood from the latent heat flux variation. Cooler SST observed from 5 December onwards also possible to explain to an extent using LHF values. But it may be noted that the SST remained cool during the period from 1 to 4 December even with reduced latent heat loss. Analysis of SWR and net heat flux further confirmed this.

In Fig. 5b we show the SWR and the deep cloud fraction estimated from AVHRR. SWR is generally low due to the high cloud fraction during the stages 2 and 3 of MJO2. But decrease of cloud fraction

from ~90% to 10% immediately after the convective stage of MJO2 increased SWR from ~140 W m^{-2} to ~ 230 W m^{-2} on December 4. This implies that the role of cloud cover and an associated decrease in SWR can be ruled out as a possible reason for the SST cooling observed from 1 December to 4 December. Moreover as it can be seen from Fig. 7c the net heat flux is positive during these days which mean that the ocean gained heat from surface fluxes. In situ observations from RV also support these findings (Moum et al., 2013). This compels to seek for the possible cause for the observed SST cooling from entrainment of colder subsurface water.

Atmospheric boundary layer structure observed in LASP/DYNAMO: The presence of strong convective activities results in significant modifications to the boundary layer, one of the effects is the presence of the cold pool, an effect of precipitation evaporation. In FY12 effort, we identified all dropsonde profiles under convection and non-convective regions and identified a general magnitude of the cold pool of less than 5^{o}C over the LASP/DYNAMO region. We further found that that boundary layer may have a double-layered structure in an otherwise well-mixed boundary layer of about 200 m in depth. We further found that about 75% of the two-layered boundary layer occurred under active convection, further illustrating the role of precipitation in modifying the boundary layer vertical structure. Two examples of the well-mixed and the two-layered structure are shown in Fig. 8. Figure 9 shows the comparison between the surface lifting condensation level (LCL) and boundary layer height identified from the soundings. We can see that the single layered boundary layer height correlates well with LCL, suggesting a well-mixed boundary layer. In the case of a two-layered structure, neither the top layer nor the bottom layer is correlated with the surface LCL, suggesting that both layers are not results of surface driving mixing.

Air-Sea temperature difference and sensible heat flux: Air sea temperature difference (ASTD) under convective and non-convective regimes was studied using co-located pairs of dropsonde and AXBT/AXCTD (Fig. 10a) from nine DYNAMO flights. Generally, ASTD was the largest under the convection than non-convection (Fig. 10b). Under convection, ASTD was the largest during the suppressed phase of MJO and decreased to minimum soon after the active phase of MJO (Fig. 10b). At the end of MJO2, no apparent differences in ASTD are seen in the convective and non-convection regions. Figures 10c and 10d shows that the large ASTD under convection during suppressed phase of MJO was mainly attributed to the low air temperature, suggesting stronger cold pool from convective precipitation before the MJO active phase. The resultant sensible (Fig. 10e) and latent heat (Fig. 10f) are given in based on the observed air-sea temperature, near-surface wind speed, assumption of saturation at the surface and using the COARE bulk algorithm. It is seen that the largest sensible heat flux was observed under convection in the suppressed phase of the November MJO and decrease towards the end of the MJO active phase. The difference in the latent heat flux in different stages of MJO and between the convective and non-convective cases are comparatively small. These results, especially those for sensible heat flux seem be different from what was observed during TOGA COARE (Lin and Johnson 1996). The implication of this variability to the MJO development over the Indian Ocean needs to be further explored.

IMPACT/APPLICATIONS

The ocean of the tropical ocean has largely been unexplored, especially relative to the MJO development and its coupled interaction with the marine atmospheric boundary layer. Our research conducted in this year intended to reveal the spatial and temporal variability in this region and understand its connection to the evolution of the MJO as a larger scale forcing environment. Our results indicate the role of convection and its associated cold pool process in enhancing the air-sea

sensible heat flux. The integrated impact for heat flux over the tropical Indian Ocean will be examined in the following year's effort by taking into consideration of the fractional coverage of extensive convection in the active and pre-active stages of the MJO. Furthermore, these results also prompt us to evaluate model parameterized sensible heat flux in forecast models where the effect of active convection and the cold pool are not taken into considerations.

As a result of the NRL effort in this project, the directly measured and derived solar and IR heating rate profiles obtained on this project provide a unique dataset that has the potential of directly characterizing the role of solar and IR radiative energy on the initiation and evolution of the MJO. This dataset is now quality controlled and shared with the broader community.

TRANSITIONS

The results from this year's research, especially the quality controlled AXBT/AXCTD datasets can be used for coupled model evaluation and diagnoses and identify model deficiencies for future improvements.

RELATED PROJECTS

None.

REFERENCES

Johnson, R. H., and P. E. Ciesielski, 2013: Structure and properties of Madden-Julian Oscillations deduced from DYNAMO sounding arrays. *J. Atmos. Sci.*, (in press).

Lin, X., and R.H. Johnson, 1996: Kinematic and thermodynamic characteristics of the flow over the Western Pacific Warm Pool during TOGA/COARE. *J. Atmos. Sci.*, **53**, 695-715.

Moum, J., S. P. de Szoeke, W. D. Smyth, J. B. Edson, H. L. DeWitt, A. J. Moulin, E. J. Thompson, C. J. Zappa, S. Rutledge, R. H. Johnson, and C. W. Fairall, 2013: Air-sea interactions from westerly wind bursts during the November 2011 MJO in the Indian Ocean. *Bull. Amer. Met. Soc.*, submitted.

Shinoda, T., T. G. Jensen, M. Flatau, S. Chen, W. Han, and C. Wang, 2013: Large-scale oceanic variability associated with the Madden-Julian Oscillation during the CINDY/DYNAMO field campaign from satellite observations. *Remote Sens.*, **5**, 2072-2092.

PUBLICATIONS

Wang, Q, D. P. Alappattu, J. A. Kalogiros, D. P. Trampp, T. G. Jensen, and R. C. Cherrett, 2013: Upper ocean characteristics observed in DYNAMO using air-deployable sono buoys, submitted to *J. Phys. Oceanogr.*

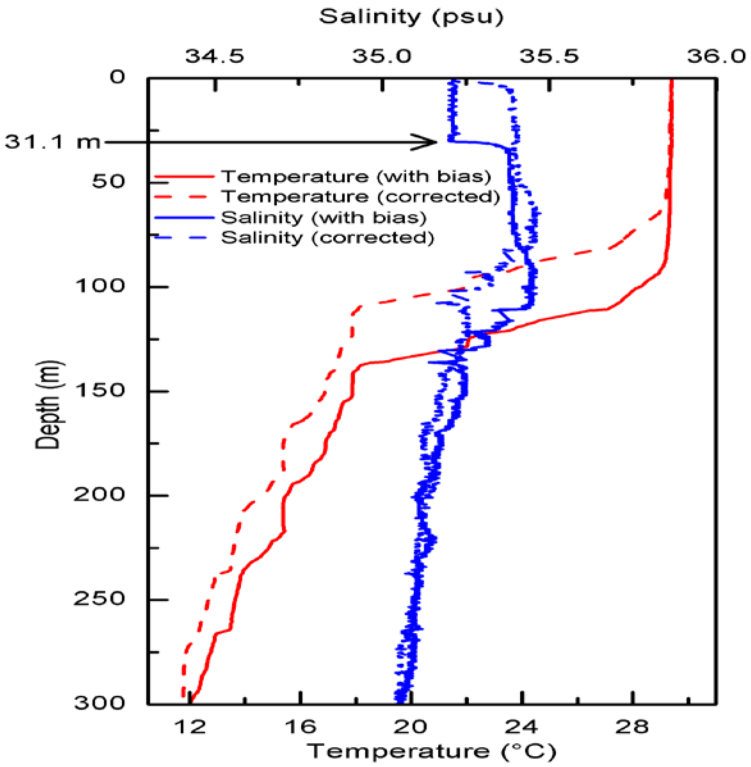

Figure 1: An example of AXCTD temperature and salinity profiles before and after depth bias correction.

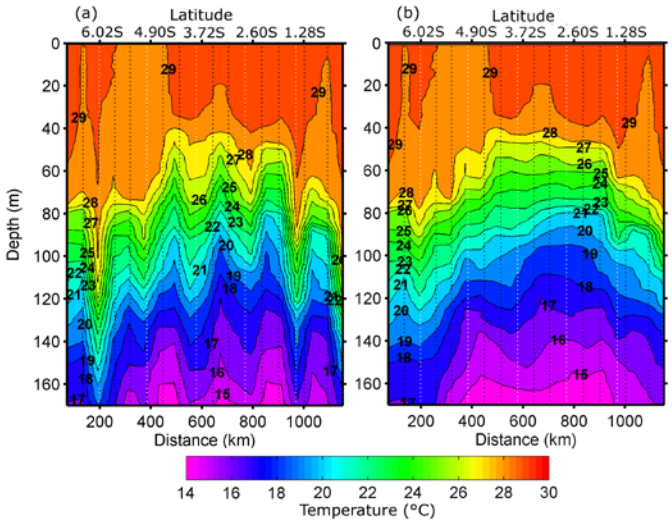

Figure 2. Vertical cross-section of temperature along the diagonal transect from Diego Garcia to R/V Revelle. (a) using profiles from AXBTs and AXCTDs without depth bias correction and (b) using same profiles corrected for depth bias. Positions of AXBT and AXCTD drops relative to DG are shown by black and white dotted lines.

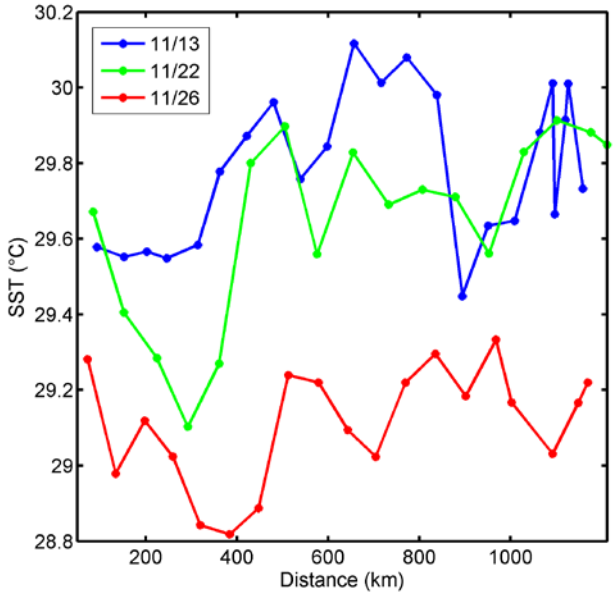

Figure 3. (a) Variability of SST from DG to RV on 13, 22 and 26 November 2011 representing stage 1 (blue), stage 2 (green) and stage 3 (red) of MJO2. The origin of the horizontal axis is at Diego Garcia.

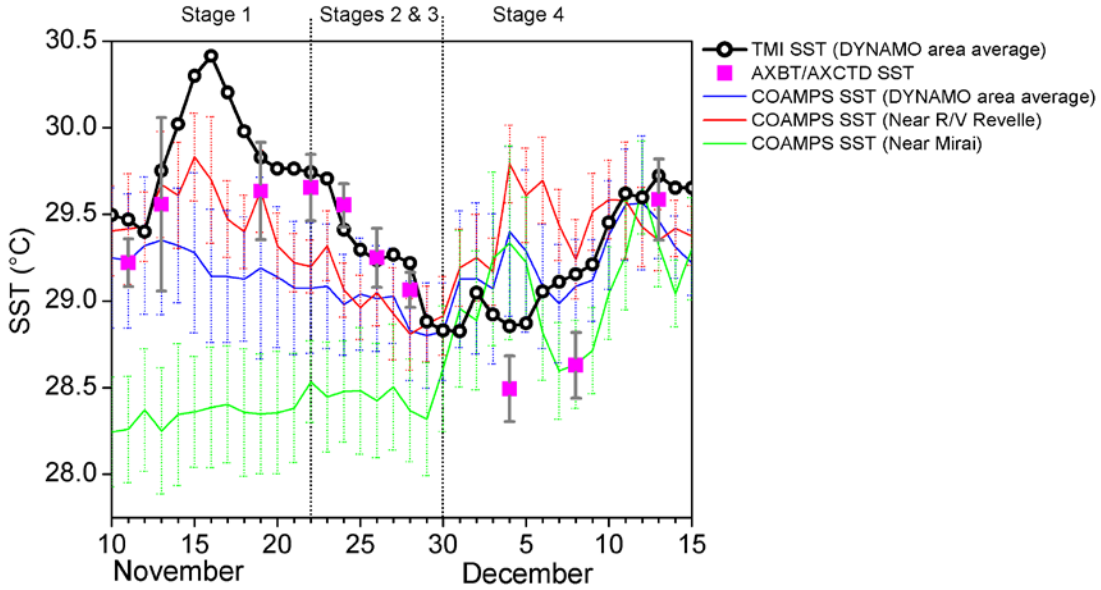

Figure 4. DYNAMO area averaged TMI SST, the SST estimated from AXBT/AXCTD temperature profiles averaged for the days of observation, DYNAMO area averaged COAMPS SST and SST in the vicinity of R/V Revelle and Mirai . Error bars represents the standard deviation of the data.

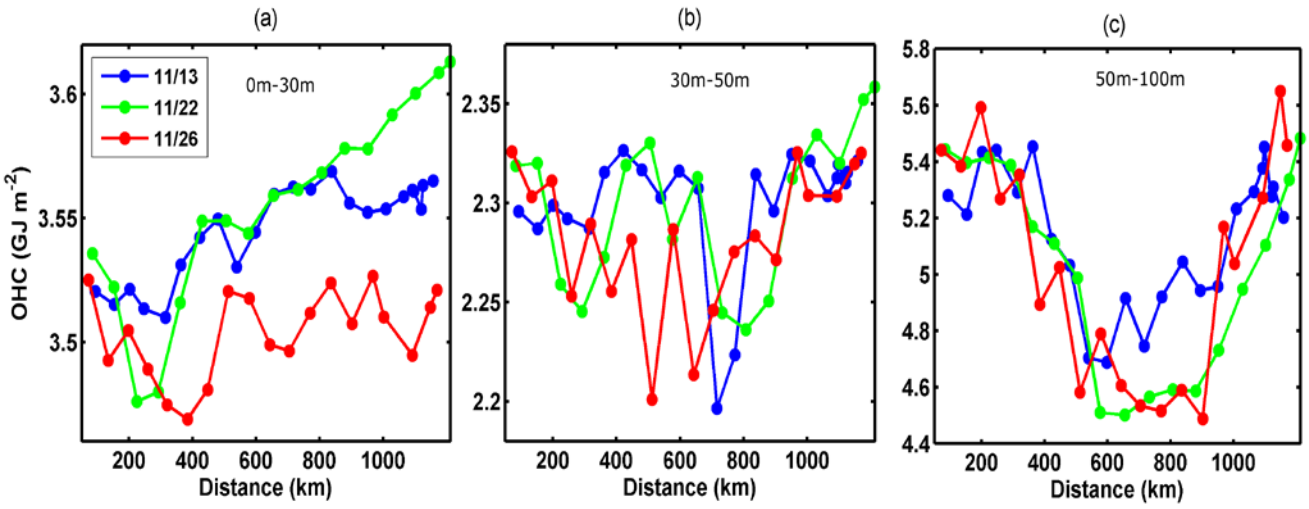

Figure 5. Ocean heat content during stage 1 (blue), stage 2 (green) and stage 3 (red) in different depth ranges: (a) from surface to 30 m depth, (b) from 30 m to 50 m depth, and (c) from 50 m to 100 m depth.

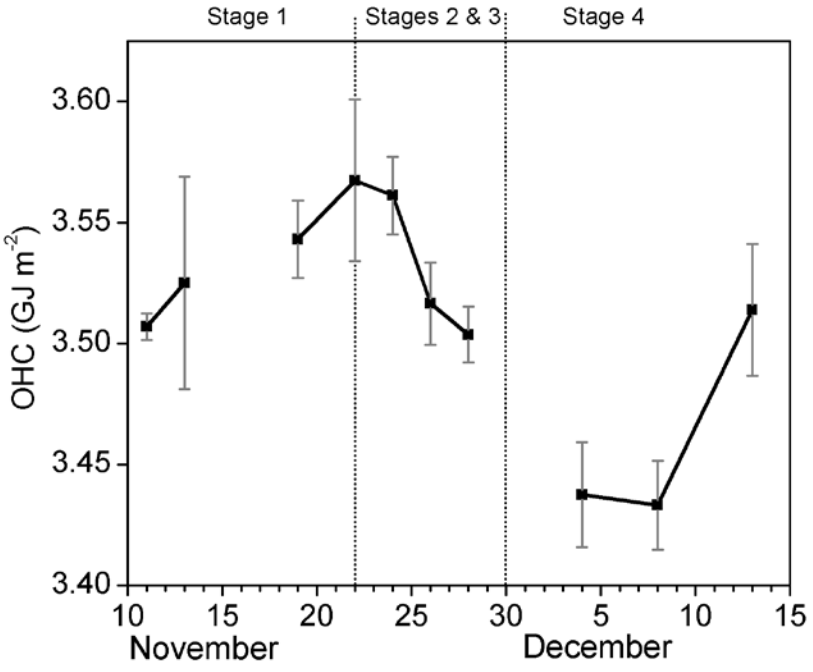

Figure 6. Mean upper 30 m oceanic heat content estimated from AXBT/AXCTD profiles.

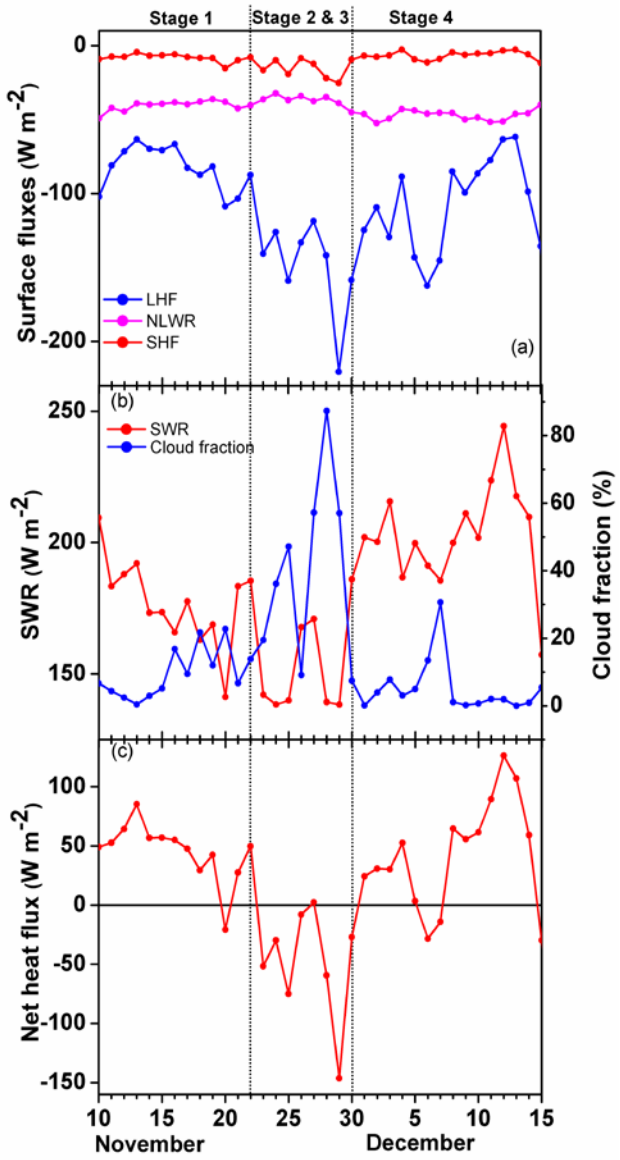

Figure 7. Domain average from NCEP-NCAR reanalysis daily products. (a) Net longwave radiation, sensible heat flux and latent heat flux (b) shortwave radiation and deep cloud fraction and (c) net heat flux.

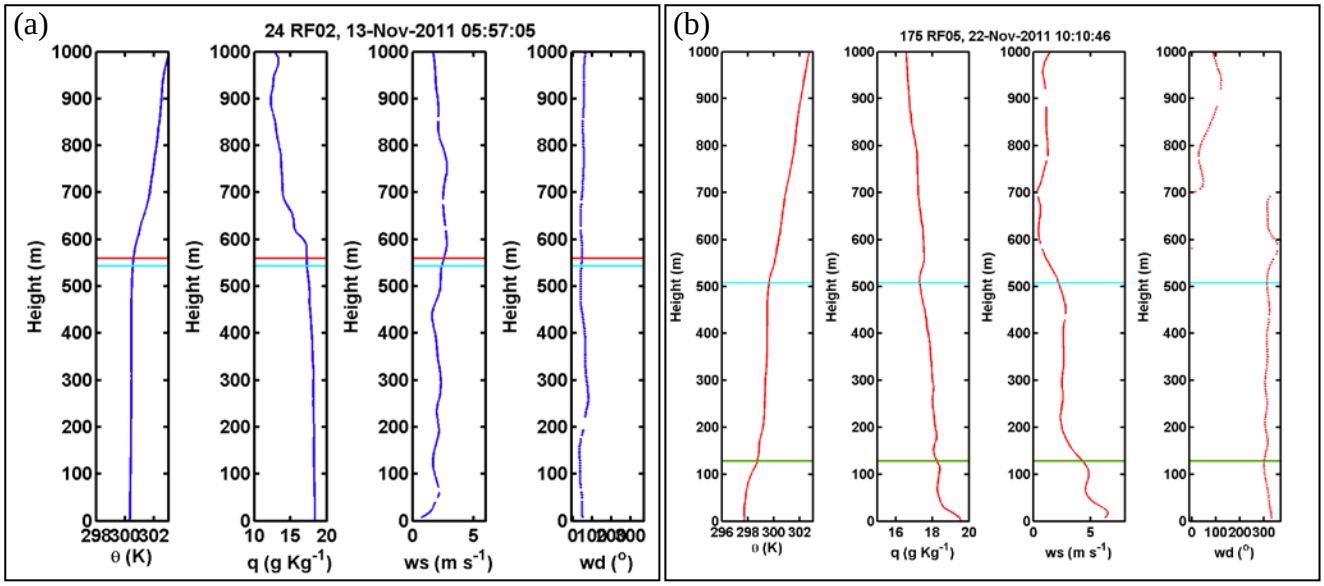

Figure 8. Typical vertical structure of the atmospheric boundary layers observed in DYNAMO.(a) Single-layered structure; (b) Double layered structure.

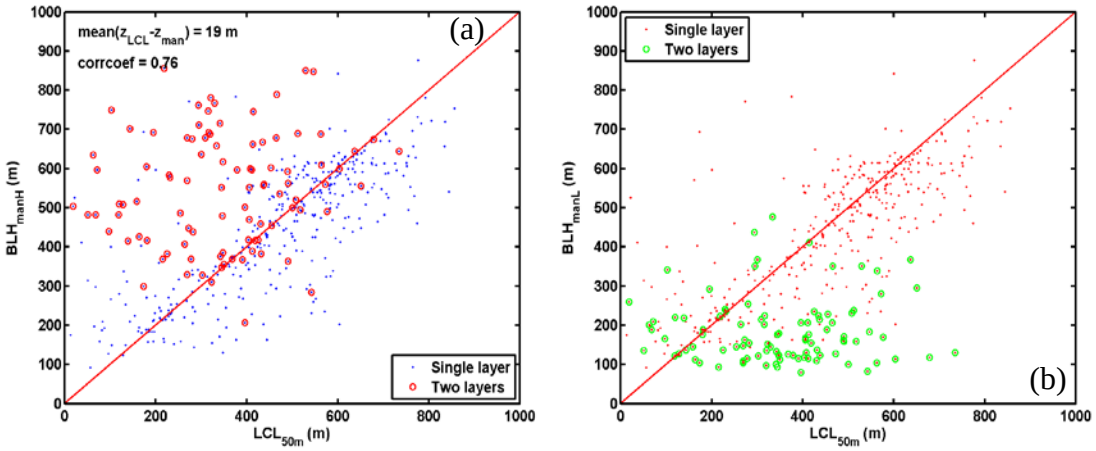

Figure 9. Boundary layer height compared to lifting condensation levels (LCL) calculated using the mean of the lowest 50 m of the dropsonde data. (a) height of the top layer is used in case of double-layered structure; (b) same as in (a), except using the bottom layer top.

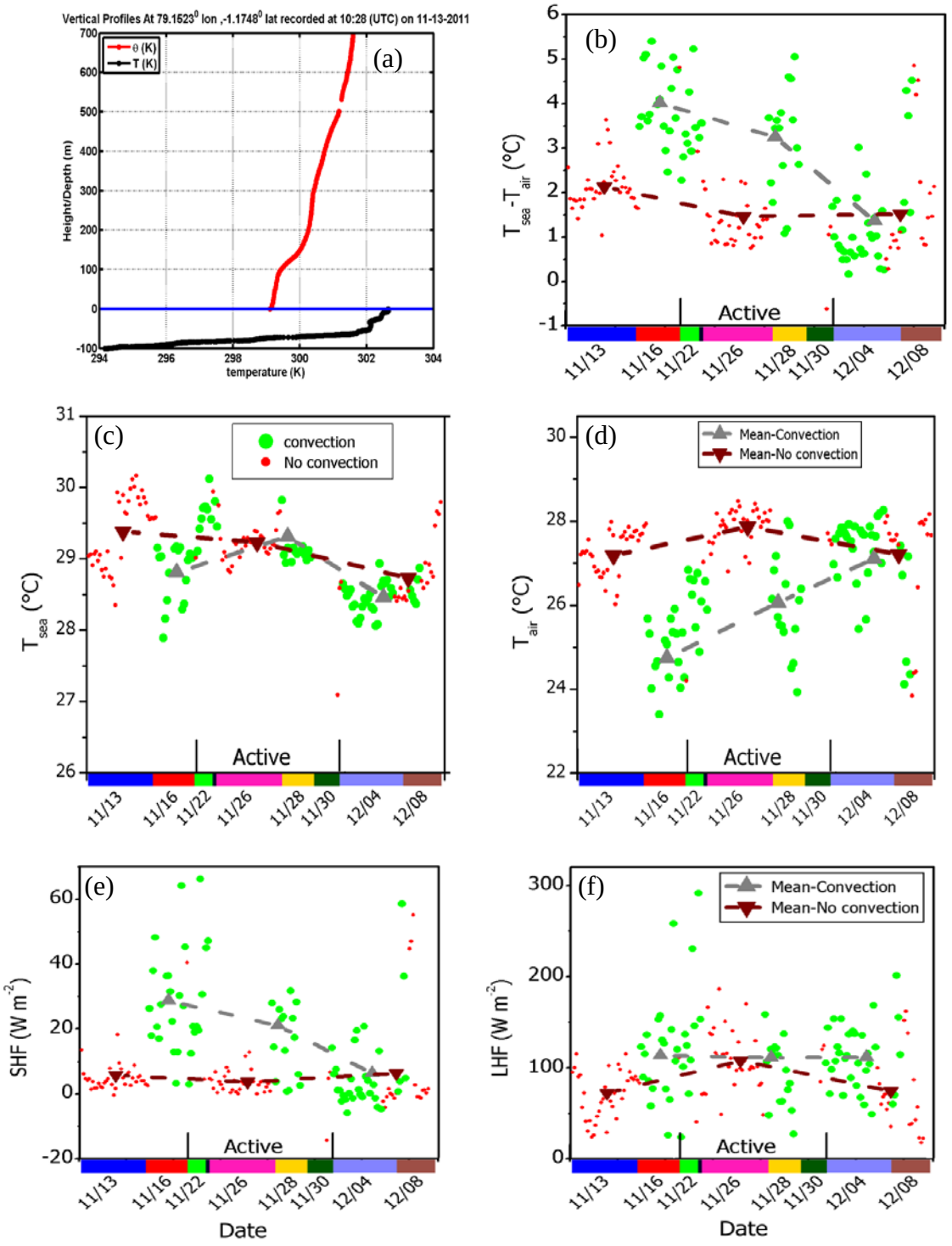

Figure 10. (a) an example of co-located dropsonde-AXBT profile pair in the atmosphere and in the ocean, (b)air-sea temperature difference, (c) sea surface temperature, (d) air temperature near the surface, (e) sensible heat flux, and (f) latent heat flux estimated using the dropsonde-AXBT/AXCTD pairs.